



Neural network method for solving nonlocal two-temperature nanoscale heat conduction in gold films exposed to ultrashort-pulsed lasers

Aniruddha Bora^a, Weizhong Dai^{a,*}, Joshua P. Wilson^a, Jacob C. Boyt^a, Sergey L. Sobolev^{b,c}

^a Mathematics & Statistics, College of Engineering & Science, Louisiana Tech University, Ruston, LA 71272, USA

^b Institute of Problems of Chemical Physics, Academy of Sciences of Russia, Chernogolovka, Moscow Region 142432, Russia

^c Samara State Technical University, ul. Molodogvardeiskaya 244, Samara 443100, Russia

ARTICLE INFO

Article history:

Received 18 September 2021

Revised 1 February 2022

Accepted 7 March 2022

Available online 19 March 2022

Keywords:

Nanoscale heat conduction

Ultrashort-pulsed laser heating

Artificial neural network method

Convergence

Thin film

ABSTRACT

Recently, we have presented an artificial neural network (ANN) method for solving the parabolic two-temperature heat conduction equations (PTTM) in double-layered thin films exposed to ultrashort-pulsed lasers. In this article, we extend this study and develop an ANN method for the nonlocal (or weakly nonlocal) two-temperature model (NTTM), which takes into account both time and space nonlocal effects when the relaxation time becomes more effective such as in low temperature and when the characteristic length scale becomes comparable with the mean free path of heat carriers such as in nano systems under femtosecond laser irradiation where the PTTM may not be suitable. We analyze the well-posedness of the NTTM and the convergence of the ANN solution to the analytical solution. The ANN method is finally used to predict the electron and lattice temperatures in nanoscale gold films when exposed to ultrashort-pulsed lasers. As compared with the experimental data, the NTTM-based ANN method gives more accurate solutions than the PTTM-based ANN method.

© 2022 Elsevier Ltd. All rights reserved.

1. Introduction

Simulation of the micro/nanoscale heat conduction induced by ultrashort-pulsed laser heating has been attracting great attention due to the wide applications of ultrashort-pulsed lasers in biology, chemistry, engineering, medicine, physics, and optical technology. We refer the readers to some references in the literature such as [1–29] and the book by Tzou [30] as well as the references therein for details.

For an ultrashort-pulsed laser, the heating involves high-rate heat flow from electrons to lattices in picosecond domains. When a metal is heated by lasers, the photon energy is primarily absorbed by the free electrons that are confined within skin depth during the excitation. Electron temperatures first shoot up to several hundreds or thousands of degrees within a few of picoseconds without significantly disturbing the metal lattices. A major portion of the thermal electron energy is then transferred to the lattices, meanwhile another part of the energy diffuses to the electrons in the deeper region of the target. Because the pulse duration is so short, the laser is turned off before thermal equilibrium between

electrons and lattices is reached. This stage is often called the non-equilibrium heating due to the large difference of temperatures between in the electrons and the lattices [7].

Following earlier models by Kagnaov et al. [31] and Anisimov et al. [32], Qiu and Tien [33–35] proposed a parabolic two-step (two-temperature) energy transport method (PTTM) based on the phonon-electron interaction to analyze heat conduction in microscale metals when energy is induced by ultrashort-pulsed laser heating. The model is expressed as follows:

$$C_e(T_e) \frac{\partial T_e}{\partial t}(x, t) = \frac{\partial}{\partial x} \left(k_e \frac{\partial T_e}{\partial x}(x, t) \right) - G[T_e(x, t) - T_l(x, t)] + Q(x, t), \quad (1a)$$

$$C_l \frac{\partial T_l}{\partial t}(x, t) = G[T_e(x, t) - T_l(x, t)], \quad (1b)$$

where T_e is the electron temperature, T_l is the lattice temperature, k_e is the conductivity, C_e and C_l are the electron heat capacity and the lattice heat capacity, respectively, G is the electron-lattice coupling factor, and $Q(x, t)$ is the energy absorption rate given by

$$Q(x, t) = Q_0 \exp\left[-\frac{x}{\delta}\right] I(t). \quad (2a)$$

* Corresponding author.

E-mail address: dai@coes.latech.edu (W. Dai).

Here, Q_0 is the intensity of the laser absorption rate, δ is the optical penetration depth, and $I(t)$ is the light intensity of the laser beam. In particular, Qiu and Tien [33–35] obtained an experimental-fitted expression of $Q(x, t)$ for thin gold films as

$$Q(x, t) = 0.94J \frac{1-R}{t_p \delta} \exp\left[-\frac{x}{\delta} - 2.77\left(\frac{t-2t_p}{t_p}\right)^2\right], \quad (2b)$$

where J is the laser fluence, R is the surface reflectivity, and t_p is the laser pulse duration in femtosecond.

As we are moving towards the era of artificial intelligence, machine and deep learning techniques are becoming a vital part in science and engineering researches. For this purpose, we have recently presented an artificial neural network (ANN) method for solving the above parabolic two-temperature heat conduction equations in double-layered thin films exposed to ultrashort-pulsed lasers [36]. The ANN method was developed based on the Physics Informed Neural Nets (PINN) method [35–68] for solving partial differential equations, particularly the combination of the Adam optimization method (a replacement of the gradient descent method) [69] and the L-BFGS (Low-memory extension of Broyden, Fletcher, Goldfarb, and Shanno) iterative method [70] for optimizing weights and biases. By starting at a small time interval to obtain the ANN solution and then using the solution at the end of that small time interval as the initial condition for the next small time interval to obtain the next ANN solution, the ANN method was able to provide accurate solutions for the case of very short-pulsed laser heating and the picosecond nonequilibrium heating stage.

As pointed out in Suslova and Hassanein [71], it has been concerned regarding the validity of the above PTM because of the delayed heat exchange between electron and lattice subsystems observed experimentally at low laser intensity when the absorbed fluence is tens of $\mu\text{J}/\text{cm}^2$. At such laser parameters, the nonequilibrium electron relaxation time in metals is comparable to electron-lattice equilibration time which is roughly few picoseconds. In such case, the assumption of an electron temperature during or immediately after the absorption of the ultrashort laser pulse in the PTM may not always be justified [72,73]. Another phenomenon commonly attributed to the ballistic motion of nonequilibrium electrons [74] is the significantly deeper heat deposition profile of the absorbed laser pulse compared to theoretical predictions of the exponential laser attenuation profile observed experimentally for different metallic targets including aluminum, copper, gold, molybdenum, nickel, silver, and tungsten [75]. In other words, ballistic electron motion and hot electron diffusion occur during the ultrashort-pulsed laser heating. As seen in FIG. 11 [76], for a laser fluence of $13.4 \text{ (J/m}^2\text{)}$, the normalized electron temperature at $x = 0$ obtained based on the PTM does not match very well with experimental data after $t = 2 \text{ (ps)}$.

For the above reasons, Sobolev [77] has recently generalized the PTM and the hyperbolic two-temperature model (HTM) [26,27,78–81] to a nonlocal two-temperature model (NTTM), which takes into account both time and space nonlocal effects [82] when the characteristic time scale becomes comparable with the mean free time (relaxation time) of heat carriers and when the characteristic length scale becomes comparable with the mean free path of heat carriers such as in nano systems under femtosecond laser irradiation. The NTTM can be expressed in heat flux and two temperatures with relaxation time and mean free path as

$$q(x, t) + \tau \frac{\partial q}{\partial t}(x, t) = -k \frac{\partial T_1}{\partial x}(x, t) + l_e^2 \frac{\partial^2 q}{\partial x^2}(x, t), \quad (3a)$$

$$C_1 \frac{\partial T_1}{\partial t}(x, t) = -\frac{\partial q}{\partial x}(x, t) + \alpha[T_2(x, t) - T_1(x, t)] + Q(x, t), \quad (3b)$$

$$C_2 \frac{\partial T_2}{\partial t}(x, t) = \alpha[T_1(x, t) - T_2(x, t)], \quad (3c)$$

where τ , l_e , C_1 and T_1 are the relaxation time, mean free path, heat capacity and temperature for electrons, respectively; C_2 and T_2 are the heat capacity and temperature for lattice, respectively; α is the electron-lattice coupling factor; k is the thermal conductivity of the material; and Q is the heat source term. When $\tau = l_e = 0$, Eq. (3) can be reduced to Eq. (1) by eliminating q .

It should be pointed out that Eq. (3a) is an equation of the Guyer–Krumhansl-type [83] in which the main merit is to emphasize the role of space nonlocal effects in heat transport [15,77,81,82,84,85]. The similar nonlocal term arises also in the extended irreversible thermodynamics that incorporates nonlocal effects by appealing to a hierarchy of higher order fluxes [18,82,85], while from the kinetic point of view, this corresponds to selecting higher-order moments of the distribution function as variables. The space nonlocal term appears also in mass transfer theory due to diffusion-stress coupling [81]. The nonlocal effects play an important role on short space scale, particularly during heat transport in nano devices, when the size of the system under consideration is comparable to the mean free path of the energy carriers or even smaller. In these situations, local equilibrium is not achieved, and therefore, generalized transport equations describing the nonlocal effects must be used instead of the classical transport equations [18,77,78,80–82,84,85]. Furthermore, it should be pointed out that for the last term in Eq. (3a) which describes space nonlocality, some researchers [15,82,85–89] called it “nonlocality” and others [90,91] called it “weak nonlocality”. In this article, we use the word “nonlocality” so that we can abbreviate the model as “NTTM” versus “PTM”.

As aforementioned above, the ultrashort-pulsed laser heating has been widely applied in many places. Under ultrashort laser irradiation of nano films, the heat transport is far from local equilibrium and, consequently, cannot be described by classical Fourier law. This is confirmed by many experimental and theoretical investigations. Thus, the advantage of the NTTM, that takes into account both time and space nonlocal effects, makes the model more effective to describe many problems in material science, such as the metal thin film thermal process induced by ultrashort-pulsed laser heating, modeling ultrafast laser ablation [92], additive manufacturing [93], and optical signal processing in telecommunications [94].

In this article, we extend our ANN study to the NTTM case and present an ANN method for solving the nonlocal two-temperature heat conduction equations in nanoscale thin gold films exposed to ultrashort-pulsed lasers, which will match well the experimental data in FIG. 11 given in Qiu et al. [76]. The rest of the article is organized as follows. In Section 2, we consider the NTTM and analyze its well-posedness. In Section 3, we propose the ANN method and its algorithm for solving the nonlocal two-temperature heat conduction equations in nanoscale thin gold films exposed to ultrashort-pulsed lasers. In Section 4, we analyze theoretically the convergence of the ANN solution to the analytical solution. In Section 5, we test the ANN method for predicting the electron and lattice temperatures in gold thin films exposed to ultrashort-pulsed lasers. Finally, we give some conclusions in Section 6.

2. Nonlocal two-temperature model

Consider the NTTM for nanoscale gold thin films exposed to the ultrashort-pulsed laser heating as

$$q(x, t) + \tau \frac{\partial q}{\partial t}(x, t) = -k \frac{\partial T_1}{\partial x}(x, t) + l_e^2 \frac{\partial^2 q}{\partial x^2}(x, t), \quad (4a)$$

$$C_1 \frac{\partial T_1}{\partial t}(x, t) = -\frac{\partial q}{\partial x}(x, t) + \alpha[T_2(x, t) - T_1(x, t)] + Q(x, t), \quad (4b)$$

$$C_2 \frac{\partial T_2}{\partial t}(x, t) = \alpha[T_1(x, t) - T_2(x, t)], \quad (4c)$$

with the heat source (since only gold thin films are considered, we use Eq. (2b) directly)

$$Q(x, t) = 0.94J \frac{1-R}{t_p \delta_{eff}} \exp\left[-\frac{x}{\delta_{eff}} - 2.77\left(\frac{t-2t_p}{t_p}\right)^2\right], \quad (5)$$

and initial and boundary conditions

$$q(x, 0) = 0, \quad T_1(x, 0) = T_0, \quad T_2(x, 0) = T_0; \quad q(0, t) = q(x_L, t) = 0. \quad (6)$$

Here, $0 \leq x \leq x_L$, $0 \leq t \leq t_T$; T_0 is the ambient temperature; $C_1 = C_{e0} \frac{T_1}{T_0}$, and $k = k_{e0} \frac{T_1}{T_0}$ where C_{e0} and k_{e0} are constant heat capacity and conductivity, respectively; and $\delta_{eff} = \delta_p + \delta_{bal}$ where δ_p is the optical penetration depth and δ_{bal} is ballistic absorption range.

We now seek an energy-type estimate for the above NTM in Eqs. (4)–(6). For simplicity, we assume those thermal parameters τ , l_e , C_1 , C_2 , k to be constants. Thus, we multiply Eq. (4a) by $\frac{1}{k}q$, Eq. (4b) by T_1 , and Eq. (4c) by T_2 , and then integrate the results over $[0, x_L]$. This gives

$$\frac{1}{k} \int_0^{x_L} q^2 dx + \frac{\tau}{2k} \frac{d}{dt} \int_0^{x_L} q^2 dx = - \int_0^{x_L} \frac{\partial T_1}{\partial x} q dx + \frac{l_e^2}{k} \int_0^{x_L} \frac{\partial^2 q}{\partial x^2} q dx, \quad (7a)$$

$$C_1 \frac{1}{2} \frac{d}{dt} \int_0^{x_L} T_1^2 dx = - \int_0^{x_L} \frac{\partial q}{\partial x} T_1 dx + \alpha \int_0^{x_L} (T_2 - T_1) T_1 dx + \int_0^{x_L} Q T_1 dx, \quad (7b)$$

$$C_2 \frac{1}{2} \frac{d}{dt} \int_0^{x_L} T_2^2 dx = \alpha \int_0^{x_L} (T_1 - T_2) T_2 dx. \quad (7c)$$

Using the integration by parts and the boundary condition in Eq. (6), we obtain

$$\begin{aligned} \int_0^{x_L} \frac{\partial T_1}{\partial x} q dx &= \int_0^{x_L} \frac{\partial}{\partial x} (T_1 q) dx - \int_0^{x_L} T_1 \frac{\partial q}{\partial x} dx \\ &= (T_1 q)|_0^{x_L} - \int_0^{x_L} T_1 \frac{\partial q}{\partial x} dx = - \int_0^{x_L} T_1 \frac{\partial q}{\partial x} dx, \end{aligned} \quad (8a)$$

$$\begin{aligned} \int_0^{x_L} \frac{\partial^2 q}{\partial x^2} q dx &= \int_0^{x_L} \frac{\partial}{\partial x} \left(\frac{\partial q}{\partial x} q \right) dx - \int_0^{x_L} \left(\frac{\partial q}{\partial x} \right)^2 dx \\ &= \left(\frac{\partial q}{\partial x} q \right)|_0^{x_L} - \int_0^{x_L} \left(\frac{\partial q}{\partial x} \right)^2 dx = - \int_0^{x_L} \left(\frac{\partial q}{\partial x} \right)^2 dx. \end{aligned} \quad (8b)$$

Substituting Eq. (8) into Eq. (7a), then summing Eq. (7a)–(7c), we obtain

$$\begin{aligned} \frac{d}{dt} \left[\frac{\tau}{2k} \int_0^{x_L} q^2 dx + \frac{C_1}{2} \int_0^{x_L} T_1^2 dx + \frac{C_2}{2} \int_0^{x_L} T_2^2 dx \right] + \frac{1}{k} \int_0^{x_L} q^2 dx \\ + \frac{l_e^2}{k} \int_0^{x_L} \left(\frac{\partial q}{\partial x} \right)^2 dx + \alpha \int_0^{x_L} (T_1 - T_2)^2 dx = \int_0^{x_L} Q T_1 dx. \end{aligned} \quad (9)$$

Using the Cauchy–Schwarz inequality ($2ab \leq \varepsilon a^2 + \frac{1}{\varepsilon} b^2$, $\varepsilon > 0$), we have

$$2 \int_0^{x_L} Q T_1 dx \leq C_1 \int_0^{x_L} T_1^2 dx + \frac{1}{C_1} \int_0^{x_L} Q^2 dx. \quad (10)$$

Multiplying Eq. (9) by 2, and using Eq. (10), we obtain

$$\begin{aligned} \frac{d}{dt} \int_0^{x_L} \left(\frac{\tau}{k} q^2 + C_1 T_1^2 + C_2 T_2^2 \right) dx + \frac{2}{k} \int_0^{x_L} q^2 dx + 2 \frac{l_e^2}{k} \int_0^{x_L} \left(\frac{\partial q}{\partial x} \right)^2 dx \\ + 2\alpha \int_0^{x_L} (T_1 - T_2)^2 dx \leq \int_0^{x_L} C_1 T_1^2 dx + \frac{1}{C_1} \int_0^{x_L} Q^2 dx. \end{aligned} \quad (11)$$

Dropping the positive-value terms on the left-hand-side of Eq. (11) and letting $E(t) = \int_0^{x_L} \left(\frac{\tau}{k} q^2 + C_1 T_1^2 + C_2 T_2^2 \right) dx$, Eq. (11) can be simplified to

$$\frac{dE(t)}{dt} \leq E(t) + \frac{1}{C_1} \int_0^{x_L} Q^2 dx, \quad (12)$$

implying that an energy-type estimate can be expressed as

$$E(t) \leq e^t [E(0) + \frac{1}{C_1} \int_0^t \int_0^{x_L} Q^2 dx dt]. \quad (13)$$

Thus, if $Q = 0$ in Eqs. (4)–(6), we define $\tilde{T}_1 = T_1 - T_0$, $\tilde{T}_2 = T_2 - T_0$. It can be seen that \tilde{T}_1 , \tilde{T}_2 , q satisfy Eqs. (4)–(6) with $Q = 0$, $q(x, 0) = 0$, $\tilde{T}_1(x, 0) = \tilde{T}_2(x, 0) = 0$, $q(0, t) = q(x_L, t) = 0$. Using the above energy-type estimate, we obtain $E(0) = 0$, $\int_0^t \int_0^{x_L} Q^2 dx dt = 0$, and hence $E(t) = \int_0^{x_L} \left(\frac{\tau}{k} q^2 + C_1 \tilde{T}_1^2 + C_2 \tilde{T}_2^2 \right) dx = 0$, implying that the homogeneous system has a solution of $T_1 = T_2 = T_0$ and $q = 0$.

Furthermore, assume that $\{T_1^{(1)}, T_2^{(1)}, q^{(1)}\}$ and $\{T_1^{(2)}, T_2^{(2)}, q^{(2)}\}$ are the solutions of Eqs. (4)–(6) obtained based on different heat sources $\{Q^{(1)}, Q^{(2)}\}$, respectively. We let $T_1 = T_1^{(1)} - T_1^{(2)}$, $T_2 = T_2^{(1)} - T_2^{(2)}$, $q = q^{(1)} - q^{(2)}$, and $Q = Q^{(1)} - Q^{(2)}$. Then, it can be seen that $\{T_1, T_2, q\}$ satisfy Eqs. (4)–(6) with $q(x, 0) = 0$, $T_1(x, 0) = T_2(x, 0) = 0$, $q(0, t) = q(x_L, t) = 0$. From Eq. (13), we obtain that $E(0) = 0$ and $E(t) \leq e^{t_T} \frac{1}{C_1} \int_0^{t_T} \int_0^{x_L} Q^2 dx dt$, where $0 \leq x \leq x_L$, $0 \leq t \leq t_T$. If $\max_{0 \leq x \leq x_L, 0 \leq t \leq t_T} |Q| \leq \varepsilon$ (a small value), then $E(t) \leq e^{t_T} \frac{1}{C_1} t_T x_L \varepsilon^2$ which is a small value, implying that the solutions $\{T_1, T_2, q\}$ are continuously dependent on Q . Hence, we conclude that the system in Eqs. (4)–(6) is well-posed.

3. Artificial neural network method for NTM

To propose an artificial neural network method for solving the system in Eqs. (4)–(6), we first make the equations in dimensionless form by introducing the following variables as follows:

$$q^* = q t_T x_L^2 10^{10}, \quad T_1^* = \frac{T_1 - T_0}{T_0}, \quad T_2^* = \frac{T_2 - T_0}{T_0}, \quad (14a)$$

$$x^* = \frac{x}{x_L}, \quad \delta^* = \frac{\delta_{eff}}{x_L}, \quad l_e^* = \frac{l_e}{x_L}, \quad t^* = \frac{t}{t_T}, \quad t_p^* = \frac{t_p}{t_T}. \quad (14b)$$

Replacing q , T_1 , T_2 , x , δ_{eff} , t , t_p , and l_e in Eqs. (4)–(6) according to Eq. (14), we have

$$q^*(x^*, t^*) + \bar{\tau} \frac{\partial q^*}{\partial t^*}(x^*, t^*) = -\bar{k} \frac{\partial T_1^*}{\partial x^*}(x^*, t^*) + (l_e^*)^2 \frac{\partial^2 q^*}{\partial (x^*)^2}(x^*, t^*), \quad (15a)$$

$$\bar{C}_1 \frac{\partial T_1^*}{\partial t^*}(x^*, t^*) = -\bar{\beta} \frac{\partial q^*}{\partial x^*}(x^*, t^*) + \bar{\alpha} [T_2^*(x^*, t^*) - T_1^*(x^*, t^*)] + \bar{Q}(x^*, t^*), \quad (15b)$$

$$\bar{C}_2 \frac{\partial T_2^*}{\partial t^*}(x^*, t^*) = \bar{\alpha} [T_1^*(x^*, t^*) - T_2^*(x^*, t^*)], \quad (15c)$$

with the heat source

$$\bar{Q}(x^*, t^*) = \frac{t_T}{T_0} 0.94J \frac{1-R}{t_p \delta^*} \exp\left[-\frac{x^*}{\delta^*} - 2.77\left(\frac{t^* - 2t_p^*}{t_p^*}\right)^2\right], \quad (16)$$

and initial and boundary conditions

$$\begin{aligned} q^*(x^*, 0) &= 0, \quad T_1^*(x^*, 0) = 0, \quad T_2^*(x^*, 0) = 0; \\ q^*(0, t^*) &= q^*(1, t^*) = 0. \end{aligned} \quad (17)$$

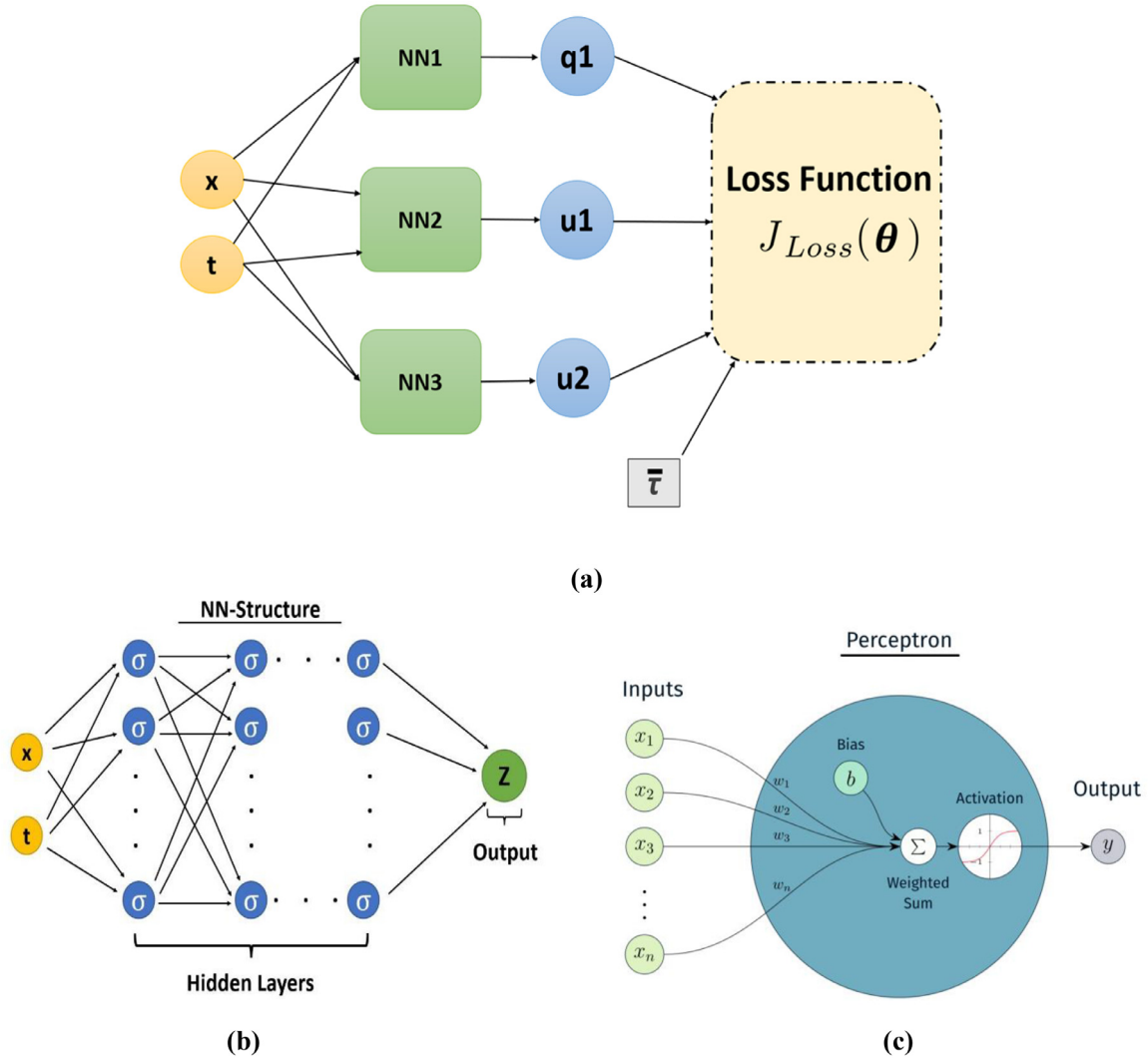


Fig. 1. Schematic diagrams of (a) the neural network used, (b) neural network structure with multi-hidden layers and multi-hidden perceptrons, and (c) a perceptron.

Here, $0 \leq x^* \leq 1$, $0 \leq t^* \leq 1$; and

$$\begin{aligned} \bar{C}_1 &= C_{e0} \frac{T_1^* + 1}{T_2^* + 1}, \quad \bar{k} = k_{e0} \frac{T_1^* + 1}{T_2^* + 1} T_0 t_T x_L 10^{10}, \\ \bar{\beta} &= \frac{1}{T_0 x_L^3 10^{10}}, \quad \bar{\alpha} = \alpha t_T, \quad \bar{\tau} = \frac{\tau}{t_T}. \end{aligned} \quad (18)$$

It should be pointed out that the factor 10^{10} in q^* is because the term $\bar{\beta}$ has x_L^3 in the denominator which is very small and therefore we multiply Eq. (4) by 10^{10} both sides to balance the values in the loss function given in Eq. (20) below, so that the iteration in our algorithm converges fast. For simplicity, we omit asterisk hereinafter.

Since there are three unknowns (i.e., q , T_1 , T_2), we design three individual neural nets NN1, NN2, NN3, and make all the neural nets to be fully connected, as shown in Fig. 1(a). Here, $q1$, $u1$, and $u2$ represent the neural network solutions for the heat flux, electron and lattice temperatures, respectively. We assume that neural nets NN1, NN2 and NN3 for $q1$, $u1$, and $u2$ have L_1 , L_2 , and L_3 numbers of hidden layers with M_1 , M_2 , and M_3 numbers of hidden perceptrons, respectively, where the typical neural net consisting of multi-hidden layers and multi-hidden perceptrons is shown in Fig. 1(b) and the configuration of perceptron is shown in Fig. 1(c). Let the input be $X = (x, t)$. The output from NN1, which is the ANN

solution $q1$, is expressed as

$$q1(x, t) = \sum_{i=1}^{M_1} W_i^{(1)} z_i^{(L_1)} + b^{(1)}, \quad (19a)$$

$$z_i^{(j)} = \sigma \left(\sum_{k=1}^{M_1} W_{k,i}^{(1,j)} z_k^{(j-1)} + b_i^{(1,j)} \right), \quad j = 2, \dots, L_1; \quad i = 1, 2, \dots, M_1; \quad (19b)$$

$$z_i^{(1)} = \sigma (W_i^{(1,0)} x + W_i^{(1,1)} t + b_i^{(1,0)}), \quad i = 1, 2, \dots, M_1; \quad (19c)$$

where σ is the activation function which is the hyperbolic tangent function (i.e., $\sigma(y) = (e^y - e^{-y}) / (e^y + e^{-y})$). Here, $W_i^{(1,0)}$, $W_i^{(1,1)}$, $W_{k,i}^{(1,j)}$, $W_i^{(1)}$, $b_i^{(1,0)}$, $b_i^{(1,j)}$, $b^{(1)}$ are weights and biases which are to be optimized. For simplicity, we list all the weights and biases into a vector and denote $\theta^{(1)} = [W_1^{(1,0)}, \dots, W_{M_1}^{(1,0)}, W_1^{(1,1)}, \dots, W_{M_1}^{(1,1)}, \dots, W_1^{(1)}, \dots, W_{M_1}^{(1)}, b_1^{(1,0)}, \dots, b_{M_1}^{(1,0)}, \dots, b^{(1)}]$. For the neural nets NN2 and NN3, we have similar expressions for $u1$, $u2$ as the above $q1$ and vectors $\theta^{(2)}$ and $\theta^{(3)}$ as sets of weights and biases for NN2 and NN3, respectively.

Note that the relaxation time for metals is usually difficult to determine [84,85,95]. In our neural network method, we consider

the dimensionless relaxation time $\bar{\tau}$ to be a parameter, which will be optimized, based on the loss function. This can be done keeping in view that to get the right value of $\bar{\tau}$ for each of the time interval, which makes the neural network method to be a combination of experimental data driven discovery with a method of solution of the partial differential equations. Let $\theta = [\theta^{(1)}, \theta^{(2)}, \theta^{(3)}, \bar{\tau}]$. We define the loss function as

$$J_{\text{Loss}}(\theta) = \text{Loss}_{\text{PDE1}} + \text{Loss}_{\text{PDE2}} + \text{Loss}_{\text{PDE3}} + \text{Loss}_{\text{IC}} + \text{Loss}_{\text{BC}} + \text{Loss}_{\text{exp}}, \quad (20)$$

where $\text{Loss}_{\text{PDE1}}$, $\text{Loss}_{\text{PDE2}}$, $\text{Loss}_{\text{PDE3}}$, Loss_{IC} , and Loss_{BC} are loss functions calculated based on PDEs in Eqs. (15) and (16), the initial condition in Eq. (17) and the boundary condition in Eq. (17), respectively. Loss_{exp} is the loss function based on the experimental data collected from FIG. 11 in Qiu et al. [76]. These loss functions are expressed in l_2 -norm as

$$\text{Loss}_{\text{IC}} = \frac{1}{N_{\text{IC}}} \sum_{i=1}^{N_{\text{IC}}} [|q1(x_i, 0) - q(x_i, 0)|^2 + |u1(x_i, 0) - T_1(x_i, 0)|^2 + |u2(x_i, 0) - T_2(x_i, 0)|^2] \quad (21a)$$

$$\text{Loss}_{\text{BC}} = \frac{1}{N_{\text{BC}}} \sum_{i=1}^{N_{\text{BC}}} [|q1(0, t_i)|^2 + |q1(1, t_i)|^2] + \frac{1}{N_{\text{BC}}} \sum_{i=1}^{N_{\text{BC}}} [|\bar{k}(u1)_x(0, t_i) - l_e^2(q1)_{xx}(0, t_i)|^2 + |\bar{k}(u1)_x(1, t_i) - l_e^2(q1)_{xx}(1, t_i)|^2], \quad (21b)$$

$$\text{Loss}_{\text{PDE1}} = \frac{1}{N_{\text{PDE}}} \sum_{i=1}^{N_{\text{PDE}}} |q1(x_i, t_i) + \bar{\tau}(q1)_t(x_i, t_i) + \bar{k}(u1)_x(x_i, t_i) - l_e^2(q1)_{xx}(x_i, t_i)|^2, \quad (21c)$$

$$\text{Loss}_{\text{PDE2}} = \frac{1}{N_{\text{PDE}}} \sum_{i=1}^{N_{\text{PDE}}} |\bar{C}_1(u1)_t(x_i, t_i) - \bar{\tau}(q1)_{tx}(x_i, t_i) - (\bar{k}(u1)_x)_x(x_i, t_i) + l_e^2(q1)_{xxx}(x_i, t_i) + \bar{\alpha}[u1(x_i, t_i) - u2(x_i, t_i)] - \bar{Q}(x_i, t_i)|^2, \quad (21d)$$

$$\text{Loss}_{\text{PDE3}} = \frac{1}{N_{\text{PDE}}} \sum_{i=1}^{N_{\text{PDE}}} |\bar{C}_2(u2)_t(x_i, t_i) - \bar{\alpha}[u1(x_i, t_i) - u2(x_i, t_i)]|^2,$$

21e

$$\text{Loss}_{\text{exp}} = \frac{1}{N_{\text{exp}}} \sum_{i=1}^{N_{\text{exp}}} |u1(0, t_i) - T_1^{(\text{exp})}(0, t_i)|^2. \quad (21f)$$

Here, $(x_i, 0)$, $(0, t_i)$, $(1, t_i)$, and (x_i, t_i) are training points which are used to obtain optimal θ (weights, biases, and $\bar{\tau}$). N_{IC} , N_{BC} , N_{PDE} , and N_{exp} are numbers of training points selected for the initial condition, the boundary condition, the PDEs, and the experimental data, respectively. $T_1^{(\text{exp})}(0, t_i)$ is given based on the experimental data in FIG. 11 in Qiu et al. [76]. It should be pointed out that in N_{BC} , we add the term $|\bar{k}(u1)_x(0, t_i) - l_e^2(q1)_{xx}(0, t_i)|^2 + |\bar{k}(u1)_x(1, t_i) - l_e^2(q1)_{xx}(1, t_i)|^2$ which is derived from Eq. (15a) by letting $q1(0, t_i) = q1(1, t_i) = 0$ based on the boundary condition Eq. (17), so that the boundary of $u1$ can be well-controlled. Furthermore, we substitute $q1(x_i, t_i)$ in Eq. (15a) into Eq. (15b) in order to calculate $u1$ more effectively.

To optimize the loss function $J_{\text{Loss}}(\theta)$ with respect to θ (weights, biases, and $\bar{\tau}$), we follow the PINN method and use a combination of the Adam optimization method and the L-BFGS method [36,69,70]. The Adam method is a gradient based optimization technique that uses adaptive estimates of lower order moments while the L-BFGS is a quasi-Newton method that uses an approximate Hessian matrix. The LBFGS optimizer has a tendency to be attracted to saddle points whereas the Adam method avoids saddle points. Hence, our approach is to combine the methods as follows: first, we use the Adam optimizer for a certain number of steps, then we use the L-BFGS optimizer to obtain higher-order convergence. As pointed out in Bora et al. [36], because the pulse duration is very short, an accurate solution requires the random

training points to be able to encapsulate the pulse in order to obtain the accurate solution. Here, we follow the idea in our previous study [36] and divide the whole time interval into several sub-intervals firstly. Once the results are obtained from the simulation of the first sub-interval, we then use it as the initial condition for the second time interval and continue the process until the whole time interval is completed. The overall procedure for obtaining the neural network solutions for solving the system in Eqs. (15)–(17) can be described in the **Algorithm** below detailed.

Algorithm: ANN method for solving the nonlocal two-temperature model.

Step 1. Initialize weights, biases and $\bar{\tau}$ in θ_0 ; set maximum iteration $N_{\text{max}} = N_1 + N_2$;
randomly select training points $X = (\mathbf{x}, \mathbf{t})$ for input; calculate $J_{\text{Loss}}(\theta_0)$

Step 2. Compare with tolerance ε (or threshold)
if $J_{\text{Loss}}(\theta_0) \leq \varepsilon$ or iteration number $\geq N_{\text{max}}$ **return** θ_0
else

Step 3. **Adam optimization method**

Set α (learning rate), β_1 , β_2 (parameters), vectors $\mathbf{m}_0 = \mathbf{v}_0 = \mathbf{0}$, and $k = 0$ (iteration)

while $k \leq N_1$ **do**

$k \leftarrow k + 1$

$\mathbf{g}_1 \leftarrow \nabla_{\theta} J_{\text{Loss}}(\theta_{k-1})$; $\mathbf{m}_k \leftarrow \beta_1 \mathbf{m}_{k-1} + (1 - \beta_1) \mathbf{g}_k$; $\mathbf{v}_k \leftarrow \beta_2 \mathbf{v}_{k-1} + (1 - \beta_2) \mathbf{g}_k^2$

(∇_{θ} is the gradient operator)

$\bar{\mathbf{m}}_k \leftarrow \mathbf{m}_k / (1 - \beta_1^k)$; $\bar{\mathbf{v}}_k \leftarrow \mathbf{v}_k / (1 - \beta_2^k)$

$\theta_k \leftarrow \theta_{k-1} - \alpha \bar{\mathbf{m}}_k / (\sqrt{|\bar{\mathbf{v}}_k|} + \epsilon)$, $\epsilon = 10^{-8}$

end while and **return** θ_{N_1}

Step 4. **L-BFGS method**

Set $\bar{\theta}_0 = \theta_{N_1}$, α_i (step length), $w = \text{integer}$, $i = 0$

while $i \leq N_2$ **do**

set $\mathbf{B}_0 = \mathbf{I}$ (identity matrix) for $i = 0$ and $\mathbf{B}_0 = \frac{s_{i-1}^T r_0}{r_0^T r_0} \mathbf{I}$ for $i > 0$

(continued on next page)

$n \leftarrow \min(i, w - 1)$	
$\mathbf{B}_i \leftarrow (\mathbf{V}_{i-1}^T \dots \mathbf{V}_{i-n}^T) \mathbf{B}_0 (\mathbf{V}_{i-1-n} \dots \mathbf{V}_{i-1})$	
$+ \rho_{i-1-n} (\mathbf{V}_{i-1}^T \dots \mathbf{V}_{i-n}^T) \mathbf{S}_{i-1-n} \mathbf{S}_{i-1-n}^T (\mathbf{V}_{i-n} \dots \mathbf{V}_{i-1})$	
$+ \rho_{i-1} (\mathbf{V}_{i-1}^T \dots \mathbf{V}_{i-n+1}^T) \mathbf{S}_{i-n} \mathbf{S}_{i-n}^T (\mathbf{V}_{i-n+1} \dots \mathbf{V}_{i-1}) + \dots +$	
$\rho_{i-1} \mathbf{S}_{i-1} \mathbf{S}_{i-1}^T$	
$\mathbf{p}_i \leftarrow -\mathbf{B}_i \nabla_{\theta} J_{\text{Loss}}(\bar{\theta}_i)$	
$\bar{\theta}_{i+1} = \bar{\theta}_i + \alpha_i \mathbf{p}_i$	
end while and return $\bar{\theta}_{N_2}$	
end if	
Step 5.	Input domain $0 \leq x \leq x_L, 0 \leq t \leq t_T$ required for prediction; output $q1, u1, u2$ and
$\bar{\tau}$ based on $\bar{\theta}_{N_2}$; transform $q1, u1, u2$ and $\bar{\tau}$ back to the solutions with dimensions	

4. Convergence analysis

Note that the neural network solutions $\{q1, u1, u2\}$ are composite functions of hyperbolic tangent function, implying these functions and their partial derivatives are continuous. We may assume that the neural network solutions $\{q1, u1, u2\}$ satisfy the following problem as

$$q1(x, t) + \bar{\tau} \frac{\partial q1}{\partial t}(x, t) = -\bar{k} \frac{\partial u1}{\partial x}(x, t) + l_e^2 \frac{\partial^2 q1}{\partial x^2}(x, t) + \phi_q(x, t), \quad (22a)$$

$$\bar{C}_1 \frac{\partial u1}{\partial t}(x, t) = -\frac{\partial q1}{\partial x}(x, t) + \bar{\alpha}[u2(x, t) - u1(x, t)] + \bar{Q}(x, t) + \phi_1(x, t), \quad (22b)$$

$$\bar{C}_2 \frac{\partial u2}{\partial t}(x, t) = \bar{\alpha}[u1(x, t) - u2(x, t)] + \phi_2(x, t), \quad (22c)$$

with initial and boundary conditions

$$q1(x, 0) = \eta_q, \quad u1(x, 0) = T_0 + \eta_1, \quad u2(x, 0) = T_0 + \eta_2, \quad (23a)$$

$$q1(0, t) = \psi_1, \quad q1(1, t) = \psi_2, \quad (23b)$$

where $0 < x < 1, 0 < t < 1$; and $\phi_q, \phi_1, \phi_2, \eta_1, \eta_2, \eta_q, \psi_1, \psi_2$ are continuous functions.

Since the output of the loss function in Eq. (20) is small in our neural network computation, we may assume that $J_{\text{Loss}}(\theta) \leq \varepsilon^2$, where $\varepsilon (> 0)$ is small. It indicates from Eq. (21) that the absolute values of these functions $\{\phi_q, \phi_1, \phi_2, \eta_1, \eta_2, \eta_q, \psi_1, \psi_2\}$ at training points are small. Since these functions are continuous and training points are selected randomly in the closed domain $\{0 \leq x \leq 1, 0 \leq t \leq 1\}$, we may assume that they satisfy

$$\max_{0 \leq x \leq 1, 0 \leq t \leq 1} \{|\phi_q|, |\phi_1|, |\phi_2|, |\eta_1|, |\eta_2|, |\eta_q|, |\psi_1|, |\psi_2|\} \leq A_0 \varepsilon, \quad (24)$$

where A_0 is a constant. This assumption is reasonable because if there is a point (x_0, t_0) such that one of these functions $\{\phi_q, \phi_1, \phi_2, \eta_1, \eta_2, \eta_q, \psi_1, \psi_2\}$ has a very large absolute value at it, we may find a small region around the point (x_0, t_0) such that this function has a large absolute value in the small region based on the continuity of the function. Since training points are randomly selected, some of the training points may fall into this small region. Thus, this function at these training points becomes very large in absolute value, which could make $J_{\text{Loss}}(\theta) \leq \varepsilon^2$ unsatisfied.

Here, we would like to show the convergence of the neural network solutions to the analytical solutions in Eqs. (15)–(17) under the assumption in Eq. (24).

Theorem. Assume that the analytical solutions $\{q, T_1, T_2\}$ have continuous first-order partial derivatives with respect to t and continuous second-order partial derivatives with respect to x , and the neural network solutions $\{q1, u1, u2\}$ are obtained based on the activation function of hyperbolic tangent function with $J_{\text{Loss}}(\theta) \leq \varepsilon^2$, where ε is a small value. Let $E_q = q1 - q$, $E_1 = u1 - T_1$ and $E_2 = u2 - T_2$. For constants $\bar{\tau}, l_e, \bar{k}, \bar{C}_1$ and \bar{C}_2 , it holds under the assumption in Eq. (24) that

$$\int_0^1 \int_0^1 [E_q^2 + E_1^2 + E_2^2] dx dt \leq A \varepsilon, \quad (25)$$

where A is a constant.

Proof. From Eqs. (15) to (17), (22) and (23), we obtain that E_q, E_1 and E_2 satisfy the following equations as

$$E_q + \bar{\tau} \frac{\partial E_q}{\partial t} = -\bar{k} \frac{\partial E_1}{\partial x} + l_e^2 \frac{\partial^2 E_q}{\partial x^2} + \phi_q, \quad (26a)$$

$$\bar{C}_1 \frac{\partial E_1}{\partial t} = -\frac{\partial E_q}{\partial x} + \bar{\alpha}(E_2 - E_1) + \phi_1, \quad (26b)$$

$$\bar{C}_2 \frac{\partial E_2}{\partial t} = \bar{\alpha}(E_1 - E_2) + \phi_2, \quad (26c)$$

with initial and boundary conditions

$$E_q(x, 0) = \eta_q, \quad E_1(x, 0) = \eta_1, \quad E_2(x, 0) = \eta_2; \\ E_q(0, t) = \psi_1, \quad E_q(1, t) = \psi_2, \quad (27)$$

where $0 \leq x \leq 1, 0 \leq t \leq 1$. We multiply Eqs. (26a)–(26c) by $\frac{1}{\bar{k}} E_q, E_1$, and E_2 , respectively, integrate them with respect to x over $[0, 1]$, and then sum the results. This gives

$$\begin{aligned} & \frac{1}{\bar{k}} \int_0^1 E_q^2 dx + \frac{\bar{\tau}}{2\bar{k}} \frac{d}{dt} \int_0^1 E_q^2 dx + \frac{\bar{C}_1}{2} \frac{d}{dt} \int_0^1 E_1^2 dx + \frac{\bar{C}_2}{2} \frac{d}{dt} \int_0^1 E_2^2 dx \\ &= - \int_0^1 \frac{\partial E_1}{\partial x} E_q dx + \frac{l_e^2}{\bar{k}} \int_0^1 \frac{\partial^2 E_q}{\partial x^2} E_q dx - \int_0^1 \frac{\partial E_q}{\partial x} E_1 dx - \bar{\alpha} \int_0^1 (E_1 - E_2) E_1 dx \\ &+ \bar{\alpha} \int_0^1 (E_1 - E_2) E_2 dx + \frac{1}{\bar{k}} \int_0^1 \phi_q E_q dx + \int_0^1 \phi_1 E_1 dx + \int_0^1 \phi_2 E_2 dx. \end{aligned} \quad (28)$$

It can be seen that

$$-\bar{\alpha} \int_0^1 (E_1 - E_2) E_1 dx + \bar{\alpha} \int_0^1 (E_1 - E_2) E_2 dx = -\bar{\alpha} \int_0^1 (E_1 - E_2)^2 dx. \quad (29)$$

Using the integration by parts, we obtain

$$\begin{aligned} \int_0^1 \frac{\partial^2 E_q}{\partial x^2} E_q dx &= \int_0^1 \frac{\partial}{\partial x} \left(\frac{\partial E_q}{\partial x} E_q \right) dx - \int_0^1 \left(\frac{\partial E_q}{\partial x} \right)^2 dx \\ &= \frac{\partial E_q}{\partial x} E_q \Big|_0^1 - \int_0^1 \left(\frac{\partial E_q}{\partial x} \right)^2 dx, \end{aligned} \quad (30a)$$

$$- \int_0^1 \frac{\partial E_1}{\partial x} E_q dx - \int_0^1 \frac{\partial E_q}{\partial x} E_1 dx = E_q E_1 \Big|_0^1. \quad (30b)$$

Substituting Eqs. (29) and (30) into Eq. (28) and then multiplying the equation by 2, we obtain

$$\begin{aligned} & 2 \frac{1}{\bar{k}} \int_0^1 E_q^2 dx + 2 \bar{\alpha} \int_0^1 (E_1 - E_2)^2 dx + 2 \frac{l_e^2}{\bar{k}} \int_0^1 \left(\frac{\partial E_q}{\partial x} \right)^2 dx \\ &+ \frac{d}{dt} \int_0^1 \left(\frac{\bar{\tau}}{\bar{k}} E_q^2 + \bar{C}_1 E_1^2 + \bar{C}_2 E_2^2 \right) dx = 2 \frac{l_e^2}{\bar{k}} \frac{\partial E_q}{\partial x} E_q \Big|_0^1 \\ &+ 2 E_q E_1 \Big|_0^1 + 2 \int_0^1 \frac{1}{\bar{k}} \phi_q E_q dx + 2 \int_0^1 \phi_1 E_1 dx + 2 \int_0^1 \phi_2 E_2 dx. \end{aligned} \quad (31)$$

Since both analytical and neural network solutions have continuous first-order partial derivatives with respect to t and continuous second-order partial derivatives with respect to x in the closed domain $\{0 \leq t \leq 1, 0 \leq x \leq 1\}$, it indicates that E_q, E_1, E_2 and their partial derivatives are continuous, and hence they are bounded in the closed domain $\{0 \leq t \leq 1, 0 \leq x \leq 1\}$. Thus, using the boundedness and Eq. (27), we obtain

$$2 \left| \frac{l_e^2}{k} \frac{\partial E_q}{\partial x} E_q \right|_0 \leq 2 \left| \frac{l_e^2}{k} (\psi_2 \frac{\partial E_q}{\partial x} |_1 - \psi_1 \frac{\partial E_q}{\partial x} |_0) \right| \leq B_1 \varepsilon, \quad (32a)$$

$$2 |E_q E_1|_0 \leq 2 [|(\psi_2 E_1)_1| + |(\psi_1 E_1)_0|] \leq B_2 \varepsilon, \quad (32b)$$

where B_1, B_2 are constants. Using the Cauchy-Schwarz inequality ($2ab \leq \varepsilon a^2 + \frac{1}{\varepsilon} b^2, \varepsilon > 0$), we obtain

$$2 \int_0^1 \frac{1}{k} \phi_q E_q dx + 2 \int_0^1 \phi_1 E_1 dx + 2 \int_0^1 \phi_2 E_2 dx \leq \int_0^1 \left[\frac{\bar{\tau}}{k} E_q^2 + \bar{C}_1 E_1^2 + \bar{C}_2 E_2^2 \right] dx + B_3 \varepsilon^2, \quad (33)$$

where $B_3 = A_0^2 (\frac{1}{\bar{\tau}} + \frac{1}{\bar{C}_1} + \frac{1}{\bar{C}_2})$. Substituting Eqs. (32) and (33) into Eq. (31) and then dropping the positive-value terms on the left-hand-side of Eq. (31), we obtain

$$\frac{d}{dt} \int_0^1 \left[\frac{\bar{\tau}}{k} E_q^2 + \bar{C}_1 E_1^2 + \bar{C}_2 E_2^2 \right] dx \leq \int_0^1 \left[\frac{\bar{\tau}}{k} E_q^2 + \bar{C}_1 E_1^2 + \bar{C}_2 E_2^2 \right] dx + (B_1 + B_2) \varepsilon + B_3 \varepsilon^2. \quad (34)$$

Denoting $D(t) = \int_0^1 (\frac{\bar{\tau}}{k} E_q^2 + \bar{C}_1 E_1^2 + \bar{C}_2 E_2^2) dx$, Eq. (34) can be simplified to

$$\frac{d}{dt} (D(t)) \leq D(t) + (B_1 + B_2) \varepsilon + B_3 \varepsilon^2, \quad (35)$$

implying that

$$D(t) \leq e^t \left\{ \int_0^t e^{-\xi} [(B_1 + B_2) \varepsilon + B_3 \varepsilon^2] d\xi + D(0) \right\} \leq e^t [(B_1 + B_2) \varepsilon + B_3 \varepsilon^2 + D(0)]. \quad (36)$$

Integrating Eq. (36) with respect to t over $[0, 1]$ we have

$$\int_0^1 D(t) dt \leq [(B_1 + B_2) \varepsilon + B_3 \varepsilon^2 + D(0)] \int_0^1 e^t dt \leq [(B_1 + B_2) \varepsilon + B_3 \varepsilon^2 + D(0)] e. \quad (37)$$

Since $\bar{\tau}, \bar{C}_1$ and \bar{C}_2 are constants, we obtain from Eq. (27) that

$$D(0) = \int_0^1 \left[\frac{\bar{\tau}}{k} \eta_q^2 + \bar{C}_1 \eta_1^2 + \bar{C}_2 \eta_2^2 \right] dx \leq B_4 \varepsilon^2, \quad (38)$$

where B_4 is a constant. Thus, from Eqs. (37), (38), we obtain

$$B_5 \left[\int_0^1 \int_0^1 (E_q^2 + E_1^2 + E_2^2) dx dt \right] \leq \int_0^1 D(t) dt \leq \varepsilon [B_1 + B_2 + B_3 \varepsilon + B_4 \varepsilon] e, \quad (39)$$

where $B_5 = \min\{\frac{\bar{\tau}}{k}, \bar{C}_1, \bar{C}_2\}$, and hence Eq. (25) is obtained where $A = \frac{1}{B_5} [B_1 + B_2 + B_3 \varepsilon + B_4 \varepsilon] e$.

5. Numerical example

To test the present artificial neural network (ANN) method for solving the nonlocal two-temperature heat conduction equations in nanoscale thin films exposed to ultrashort-pulsed lasers, we considered the thickness of gold film to be 100 (nm) and 20 (nm), respectively, where the film is exposed to an ultrashort-pulsed laser heating with the laser fluence of $J = 13.4$ (J/m²), and $R = 0.93$, $t_p = 100$ (fs), $\delta_{eff} = \delta_p = 15.3$ (nm) for the 100-nm thickness case based on the reference [76], in order to compare with FIG. 11 in

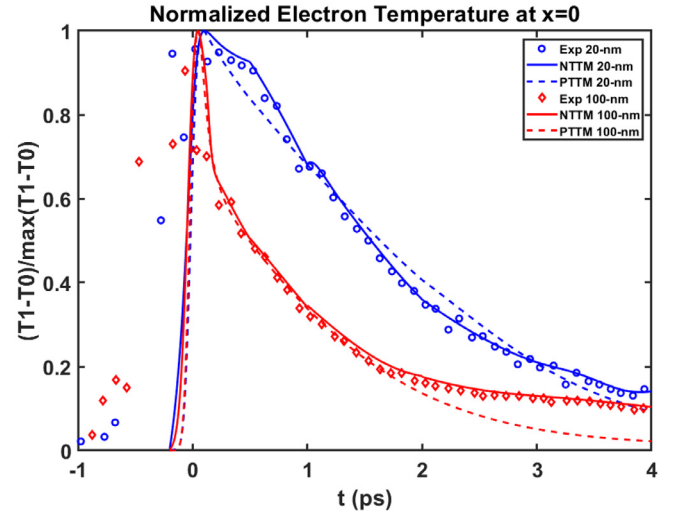


Fig. 2. Normalized electron temperatures for $x_L=100$ (nm) and 20 (nm), where results were obtained based on the neural networks for the PTTM and the NTTM, respectively, as compared with the experimental data given in [76] during 0.1 (ps) ultrashort-pulsed laser heating at a fluence of 13.4 (Jm⁻²).

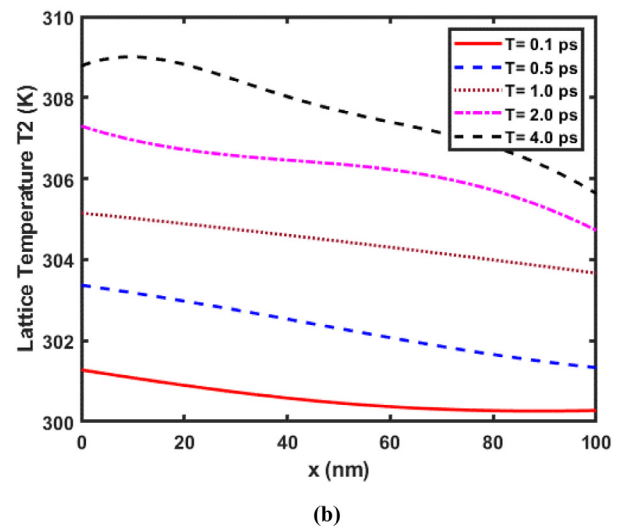
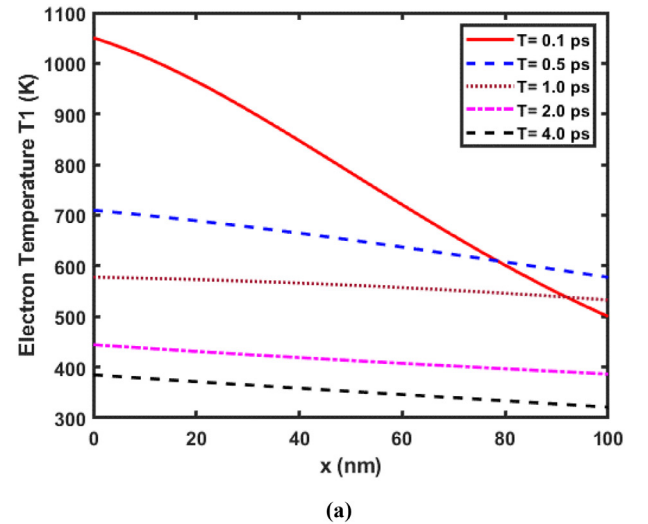
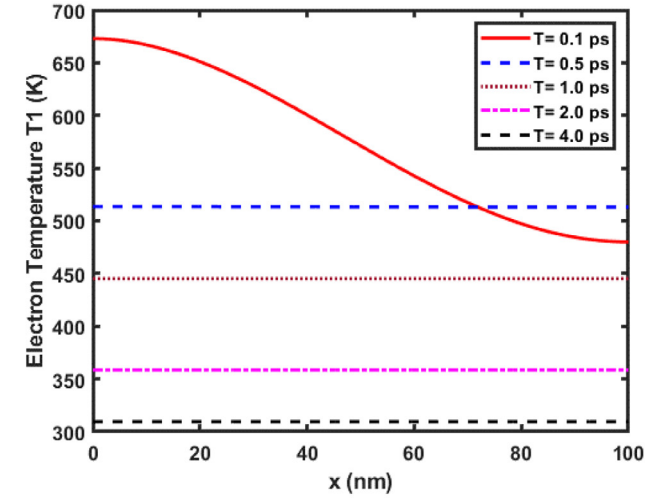
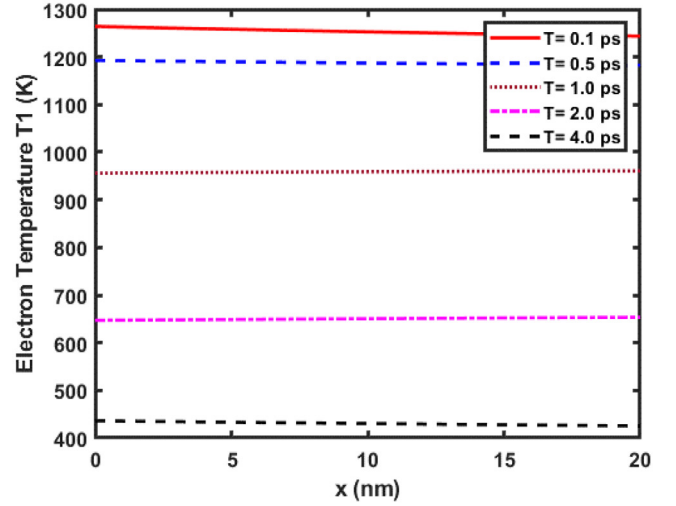


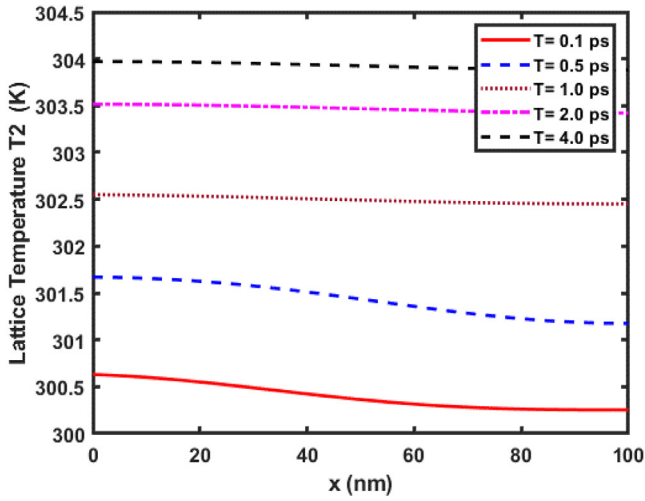
Fig. 3. Profiles of (a) electron temperature and (b) lattice temperature at various times in a 100-nm gold film during 0.1 (ps) ultrashort-pulsed laser heating at a fluence of 13.4 (Jm⁻²), which were obtained using the NTTM-based ANN method.



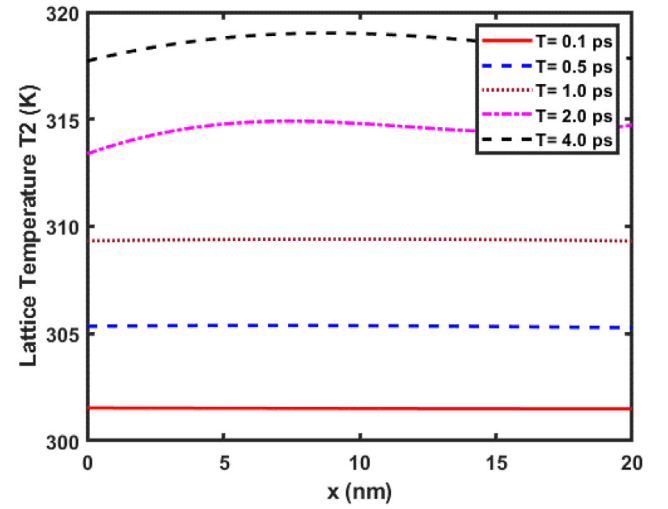
(a)



(a)



(b)



(b)

Fig. 4. Profiles of (a) electron temperature and (b) lattice temperature at various times in a 100-nm gold film during 0.1 (ps) ultrashort-pulsed laser heating at a fluence of $13.4 \text{ (Jm}^{-2}\text{)}$, which were obtained using the PTM-based ANN method.

Qiu et al. [76]. For the 20-nm thickness case, we added the ballistic penetration depth $\delta_{bal} = 105 \text{ (nm)}$ and obtained $\delta_{eff} = 120.3 \text{ (nm)}$ due to that the thickness is smaller than the mean free path and hence it may occur the ballistic motion of the electron. In our computation, we chose thermal properties of gold as follows: $C_{e0} = 2.1 \times 10^4 \text{ (Jm}^{-3} \text{ K}^{-1}\text{)}$, $C_l = 2.5 \times 10^6 \text{ (Jm}^{-3} \text{ K}^{-1}\text{)}$, $k_{e0} = 315 \text{ (Wm}^{-1} \text{ K}^{-1}\text{)}$, $G = 2.6 \times 10^{16} \text{ (Wm}^{-3} \text{ K}^{-1}\text{)}$ [76], $l_e = 37.7 \text{ (nm)}$ [96], and $T_0 = 300 \text{ (K)}$, while the relaxation time τ was kept to be a parameter determined by the loss function. In the algorithm, we chose $\varepsilon = 10^{-8}$ and $\beta_1 = 0.99$, $\beta_2 = 0.99$, $a = 10^{-4}$ for the Adam method as well as $w = 50$, $\alpha_i = 1$ for the L-BFGS method.

Two cases were solved for the NTTM and the PTM using the present ANN method. In our computation, the time interval was divided into four sub-time intervals: (i) $0 \leq t \leq 0.7 \text{ (ps)}$, (ii) $0.7 \text{ (ps)} \leq t \leq 1.2 \text{ (ps)}$, (iii) $1.2 \text{ (ps)} \leq t \leq 2.2 \text{ (ps)}$, and (iv) $2.2 \text{ (ps)} \leq t \leq 4.2 \text{ (ps)}$. Once the solutions were obtained, we shifted the time back by $-2t_p$ to compare with the curves shown in FIG. 11 [76] since their initial conditions were set at $t = -2t_p$.

For the first time interval (i) $0 \leq t \leq 0.7 \text{ (ps)}$, we discretized x and t into 900 and 500 points, respectively. From this mesh, 50

Fig. 5. Profiles of (a) electron temperature and (b) lattice temperature at various times in a 20-nm gold film during 0.1 (ps) ultrashort-pulsed laser heating at a fluence of $13.4 \text{ (Jm}^{-2}\text{)}$, which were obtained using the NTTM-based ANN method.

training points were selected randomly for the initial and boundary. On the other hand, 10,000 random points were selected for training of the interior region. We used 8 hidden layers and 100 perceptrons each layer for all three neural networks NN1, NN2 and NN3. Number of iterations used for Adam and L-BFGS was set to be 50,000 each.

For the second time interval (ii) $0.7 \text{ (ps)} \leq t \leq 1.2 \text{ (ps)}$, we discretized x and t into 300 and 500 points, respectively. Number of training points for the initial, boundary and interior were kept the same along with neural network configuration as above. Numbers of iterations used for Adam are 50,000 and L-BFGS are 5,000, respectively.

For the third time interval (iii) $1.2 \text{ (ps)} \leq t \leq 2.2 \text{ (ps)}$, we discretized x and t in the similar way to the second time interval. For this case, 100 and 50 training points were selected randomly for the initial and boundary, respectively. On the other hand, 20,000 random points were selected for training of the interior region. The neural network configuration was kept the same as above. Number of iterations used for Adam is 50,000, but no L-BFGS was needed to use due to the variation of the temperature is small.

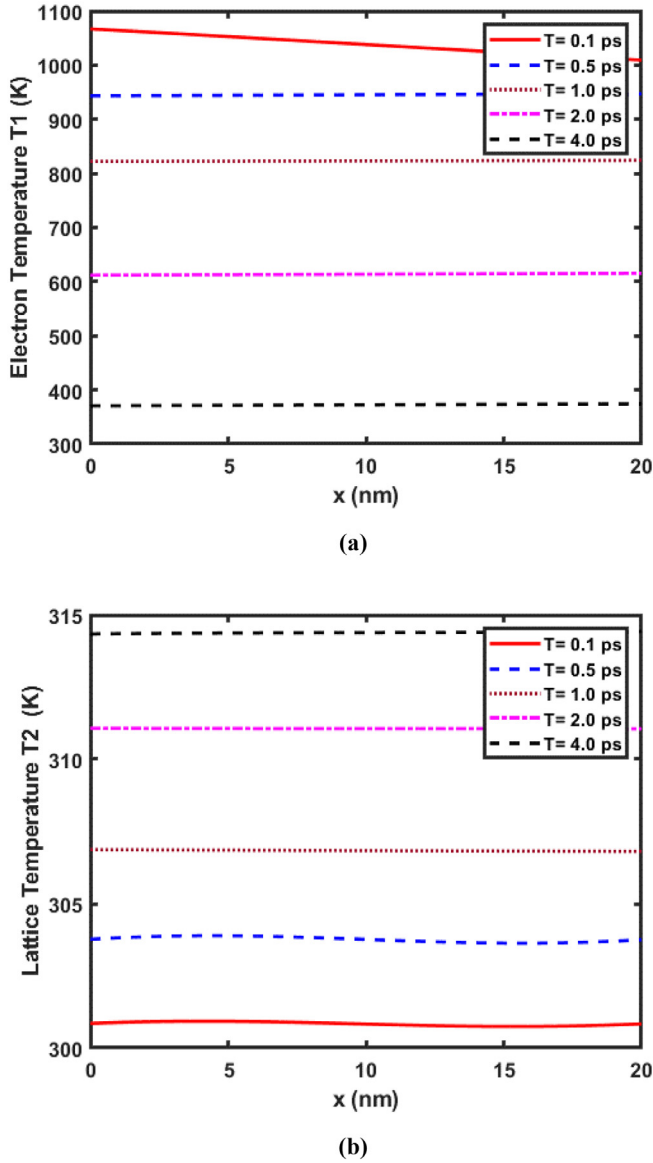


Fig. 6. Profiles of (a) electron temperature and (b) lattice temperature at various times in a 20-nm gold film during 0.1 (ps) ultrashort-pulsed laser heating at a fluence of $13.4 \text{ (Jm}^{-2}\text{)}$, which were obtained using the PTM-based ANN method.

For the fourth time interval (iv) $2.2 \text{ (ps)} \leq t \leq 4.2 \text{ (ps)}$, we discretized x and t the same way as that the third time interval case. The number of training points for the initial, boundary and interior were kept the same along with neural network configuration as above. And only Adam method was used for optimization with the same number of iterations.

The final values of loss function with the configuration discussed above were obtained as follows. For the 100-nm thickness case, the values in four time intervals obtained using the NTTM-based ANN method are $9.898\text{e-}04$, $6.820\text{e-}05$, $7.806\text{e-}05$ and $3.807\text{e-}05$, respectively, on the other hand, the values in four time intervals obtained using the PTM-based ANN method are $1.889\text{e-}06$, $1.509\text{e-}07$, $2.220\text{e-}05$ and $2.775\text{e-}06$, respectively. For the 20-nm thickness case, the values in four time intervals obtained using the NTTM-based ANN method are $6.809\text{e-}05$, $9.532\text{e-}04$, $1.589\text{e-}04$ and $3.523\text{e-}05$, respectively, on the other hand, the values in four time intervals obtained using the PTM-based ANN method are $2.451\text{e-}06$, $2.061\text{e-}07$, $4.117\text{e-}07$ and $8.677\text{e-}07$, respectively.

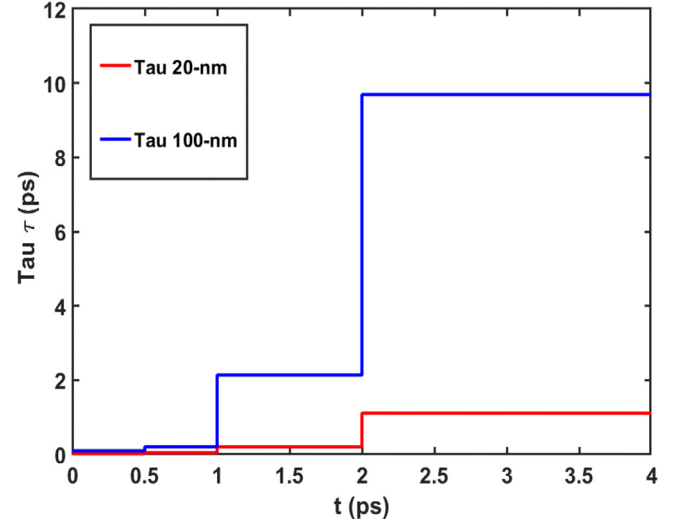


Fig. 7. Profiles of electron relaxation time τ at different range of time intervals for $x_L = 100 \text{ (nm)}$ and 20 (nm) , respectively.

Since the ANN solutions are composite functions of hyperbolic tangent function, the maximum value of the electron temperature can be easily found using the $\max()$ command in the MATLAB. We obtained the maximum value of the electron temperature T_1 as follows. For the 100-nm thickness case, $(T_1)_{\max} = 1114.0 \text{ (K)}$ at time $t = 0.2464 \text{ (ps)}$ obtained using the NTTM-based ANN method, and $(T_1)_{\max} = 729.3 \text{ (K)}$ at time $t = 0.2464 \text{ (ps)}$ obtained using the PTM-based ANN method. For the 20-nm thickness case, $(T_1)_{\max} = 1264.3 \text{ (K)}$ at time $t = 0.3050 \text{ (ps)}$ obtained using the NTTM-based ANN method, and $(T_1)_{\max} = 1068.0 \text{ (K)}$ at time $t = 0.2912 \text{ (ps)}$ obtained using the PTM-based ANN method.

To compare with the experimental values at $x = 0$ within $0 \text{ (ps)} \leq t \leq 4.0 \text{ (ps)}$, which was given in FIG. 11 [76], we calculated the normalized electron temperature at $x = 0$ as $(T_1 - T_0) / ((T_1)_{\max} - T_0)$ and plotted the profiles in Fig. 2. It can be seen that the normalized electron temperatures obtained using the NTTM-based ANN method agree very well with the experimental values, and they are better than those obtained using the PTM-based ANN method. Furthermore, the normalized electron temperatures obtained using the PTM-based ANN method are the same as those obtained in FIG. 11 [76]. It should be pointed out that the experimental $(T_1^{\text{exp}})_{\max}$ was not provided in Qiu et al. [76], and therefore, we replaced it with $(T_1)_{\max}$ obtained using the PTM-based ANN method. That may be the reason why the values of loss function obtained using the PTM-based ANN method are much smaller than those obtained using the NTTM-based ANN method.

Figs. 3 and 4 show the electron and lattice temperature profiles at various times along the thickness direction for the 100-nm thickness case obtained using the NTTM-based ANN method and the PTM-based ANN method, respectively. Figs. 5 and 6 show the electron and lattice temperature profiles at various times along the thickness direction for the 20-nm thickness case obtained using the NTTM-based ANN method and the PTM-based ANN method, respectively.

From our NTTM-based ANN method, we obtained values of the relaxation time τ in the aforementioned four time intervals as shown in Fig. 7. It can be seen from Fig. 7 that the relaxation time τ obtained using the NTTM-based ANN method increases with time t , particularly after $t = 2 \text{ (ps)}$. Here is our explanation for the interesting phenomenon. Note that the relaxation time τ is defined as $\tau = \frac{\mu}{v^2}$, where μ is the thermal diffusivity and v is the thermal wave speed. From Fig. 2, we see that for the 20-nm thickness case, the curve from the experimental data decreases slowly

after $t = 3$ (ps). It probably indicates that the thermal wave speed is slow when the electron temperature tends to steady-state, implying that τ increases. For the 100-nm thickness case, the curve from the experimental data is almost flat after $t = 2$ (ps). It probably indicates that the thermal wave speed is much slow, implying that τ should increase a lot after $t = 2$ (ps). Fig. 7 shows that the relaxation time τ , which was obtained using the NTTM-based ANN method, reflects such phenomenon observed from the experimental data. This result further confirms the advantage of the NTTM over the PTM.

6. Conclusion

In this study, we have presented an artificial neural network (ANN) method for solving the nonlocal (or weakly nonlocal) two-temperature heat conduction equations in gold thin films exposed to ultrashort-pulsed lasers. The nonlocal two-temperature model (NTTM) takes into account both time and space nonlocal effects when the relaxation time becomes more effective such as in low temperature and when the characteristic length scale becomes comparable with the mean free path of heat carriers such as in nano systems under femtosecond laser irradiation where the PTM may not be suitable. We have theoretically analyzed the well-posedness of the NTTM and the convergence of the ANN solution to the analytical solution. The ANN method has been tested to predict the electron and lattice temperatures in nanoscale gold films (both 100-nm and 20-nm in thickness) when exposed to ultrashort-pulsed lasers. As compared with the experimental data, the NTTM-based ANN method gives more accurate solution than the PTM-based ANN method. Results show that the present ANN method for the NTTM is promising.

It should be pointed out that the present NTTM-based ANN method and its algorithm can be easily extended to three-dimensional cases or to deal with the nonlocal N-temperature model where there are N energy carriers in the materials such as cells exposed to ultrashort-pulsed lasers [97–99]. In particular, when N is large, solving the N-temperature model using the common numerical methods could be very tedious. However, the present NTTM-based ANN method can solve the N-temperature model much effectively with the aid of the GPU computing.

Declaration of Competing Interest

Authors declare that they have no conflict of interest.

CRediT authorship contribution statement

Aniruddha Bora: Methodology, Software, Data curation, Writing – original draft, Visualization. **Weizhong Dai:** Conceptualization, Methodology, Formal analysis, Writing – review & editing, Supervision. **Joshua P. Wilson:** Methodology, Software, Writing – review & editing. **Jacob C. Boyt:** Methodology, Software. **Sergey L. Sobolev:** Conceptualization, Methodology, Writing – review & editing.

Acknowledgements

The authors are deeply grateful to the anonymous reviewers for their valuable comments and suggestions which greatly enhance the quality of this manuscript. S.L. Sobolev was supported by a grant in accordance with the state task of Russian Federation, state registration no. A A A A -A 19-119071190017-7.

References

- [1] M.A. Al-Nimr, O.M. Haddad, V.S. Arpaci, Thermal behavior of metal films—A hyperbolic two-step model, *Heat Mass Transf.* 35 (1999) 459–464.
- [2] M.A. Al-Nimr, M. Hader, M. Naji, Use of the microscopic parabolic heat conduction model in place of the macroscopic model validation criterion under harmonic boundary heating, *Int. J. Heat Mass Transf.* 46 (2003) 333–339.
- [3] M.A. Al-Nimr, S. Kiwan, Effect of thermal losses on the microscopic two-step heat conduction model, *Int. J. Heat Mass Transf.* 43 (2001) 1013–1018.
- [4] M. Al-Odat, M.A. Al-Nimr, M. Hamdan, Thermal stability of superconductors under the effect of a two-dimensional hyperbolic heat conduction model, *Int. J. Numer. Meth. Heat Fluid Flow* 12 (2002) 163–177.
- [5] J.K. Chen, J.E. Beraun, Numerical study of ultrashort laser pulse interactions with metal films, *Numer. Heat Transf., Part A* 40 (2001) 1–20.
- [6] J.K. Chen, W.P. Latham, J.E. Beraun, Axisymmetric modeling of femtosecond-pulse laser heating on metal films, *Numer. Heat Transf., Part B* 42 (2002) 1–17.
- [7] J.K. Chen, J.E. Beraun, C.L. Tham, Investigation of thermal response caused by pulsed laser heating, *Numer. Heat Transf., Part A* 44 (2003) 705–722.
- [8] J.K. Chen, D.Y. Tzou, J.E. Beraun, Numerical investigation of ultrashort laser damage in semiconductors, *Int. J. Heat Mass Transf.* 48 (2005) 501–509.
- [9] W. Dai, C. Johnson, A new accurate finite-difference scheme for the thermal analysis of one-dimensional microspheres exposed to ultrashort-pulsed lasers, *Numer. Heat Transf., Part B* 57 (2010) 241–259.
- [10] W. Dai, T. Niu, A finite difference method for solving nonlinear hyperbolic two-step model in a double-layered thin film exposed to ultrashort pulsed lasers with nonlinear interfacial conditions, *Nonlinear Anal. Hybrid Sys.* 2 (2008) 121–143.
- [11] W. Dai, G. Li, A finite difference scheme for solving parabolic two-step micro heat transport equations in a double-layered micro sphere heated by ultrashort-pulsed lasers, *Numer. Methods Partial Differ. Equ.* 22 (2006) 1396–1417.
- [12] W. Dai, H. Song, S. Su, R. Nassar, A stable finite difference scheme for solving a hyperbolic two-step model in a 3D micro sphere exposed to ultrashort-pulsed lasers, *Int. J. Numer. Meth. Heat Fluid Flow* 16 (2006) 693–717.
- [13] W. Dai, Q. Li, R. Nassar, L. Shen, An unconditionally stable three level finite difference scheme for solving parabolic two-step micro heat transport equations in a three-dimensional double-layered thin film, *Int. J. Numer. Methods Eng.* 59 (2004) 493–509.
- [14] A. Giri, J.T. Gaskins, B.F. Donovan, C. Szejewski, R.J. Warzoha, M.A. Rodriguez, J. Ihlefeld, P.E. Hopkins, Mechanisms of nonequilibrium electron-phonon coupling and thermal conductance at interfaces, *J. Appl. Phys.* 117 (2015) 105105.
- [15] D. Jou, J. Casas-Vaizquez, G. Lebon, *Extended Irreversible Thermodynamics*, fourth ed., Springer, Berlin, 2010.
- [16] I.K. Kaba, W. Dai, A stable three-level finite difference scheme for solving the parabolic two-step model in a 3D micro-sphere heated by ultrashort-pulsed lasers, *J. Comput. Appl. Math.* 181 (2005) 125–147.
- [17] B. Kim, H.K. Nam, S. Watanabe, Selective laser ablation of metal thin films using ultrashort pulses, *Int. J. Precis. Eng. Manuf. - Green Tech.* 8 (2021) 771–782.
- [18] Y. Mao, M. Xu, Lattice Boltzmann numerical analysis of heat transfer in nano-scale silicon films induced by ultra-fast laser heating, *Int. J. Therm. Sci.* 89 (2015) 210–221.
- [19] Y. Mao, M. Xu, Non-fourier heat conduction in a thin gold film heated by an ultra-fast-laser, *Sci. China* 58 (2015) 1–12.
- [20] M. Mozafarifar, D. Toghraie, Time-fractional subdiffusion model for thin metal films under femtosecond laser pulses based on Caputo fractional derivative to examine anomalous diffusion process, *Int. J. Heat Mass Transf.* 153 (2020) 119592.
- [21] D.W. Muller, T. Fox, P.G. Grutzmacher, Applying ultrashort pulsed direct laser interference patterning for functional surfaces, *Sci. Rep.* 10 (2020) 3647.
- [22] K.M.M. Tunc, M.E. Gunay, F. Bayata, Analysis of the thermalization dynamics of two-layer thin films irradiated by femtosecond laser, *Optik* 208 (2020) 164137.
- [23] F. Ruffino, M.G. Grimaldi, Nanostructuring of thin metal films by pulsed laser irradiations: a review, *Nanomaterials (Basel)* 9 (2019) 1133.
- [24] A. Sharif, N. Farid, R.K. Vijayaraghavan, J.P. McNally, G.M. O'Connor, Femtosecond laser assisted crystallization of gold thin films, *Nanomaterials* 11 (2021) 1186.
- [25] S. Shen, W. Dai, J. Cheng, Fractional parabolic two-step model and its accurate numerical scheme for nanoscale heat conduction, *J. Comput. Appl. Math.* 375 (2020) 112812.
- [26] S.L. Sobolev, Transport processes and traveling waves in systems with local nonequilibrium, *Sov. Phys. Usp.* 34 (1991) 217–229.
- [27] S.L. Sobolev, Two-temperature discrete model for nonlocal heat conduction, *J. Phys. III France* 3 (1993) 2261–2298.
- [28] T. Xue, X. Zhang, K.K. Tamma, On a generalized non-local two-temperature heat transfer DAE modeling/simulation methodology for metal-nonlocal thermal inter-facial problems, *Int. J. Heat Mass Transf.* 138 (2019) 508–515.
- [29] S. Zhai, L. Huang, Z. Weng, W. Dai, Parabolic two-step model and accurate numerical scheme for nanoscale heat conduction induced by ultrashort-pulsed laser heating, *J. Comput. Appl. Math.* 369 (2020) 112591.
- [30] D.Y. Tzou, *Macro-to-Microscale Heat Transfer: The Lagging Behavior*, John Wiley & Sons, New York, 2015.
- [31] M.I. Kagnaov, I.M. Lifshitz, M.V. Tanatarov, Relaxation between electrons and crystalline lattices, *Sov. Phys. JETP* 4 (1957) 173–178.
- [32] S.I. Anisimov, B.L. Kapeliovich, T.L. Perelman, Electron emission from metal surfaces exposed to ultra-short laser pulses, *Sov. Phys. JETP* 39 (1974) 375–377.
- [33] T.Q. Qiu, C.L. Tien, Short-pulse laser-heating on metals, *Int. J. Heat Mass Transf.* 35 (1992) 719–726.
- [34] T.Q. Qiu, C.L. Tien, Heat transfer mechanisms during short-pulse laser heating of metals, *J. Heat Transf. (ASME)* 115 (1993) 835–841.

- [35] T.Q. Qiu, C.L. Tien, Femtosecond laser heating of multi-layer metals I. Analysis, *Int. J. Heat Mass Transf.* 37 (1994) 2789–2797.
- [36] A. Bora, W. Dai, J.P. Wilson, J.C. Boyt, Neural network method for solving parabolic two-temperature microscale heat conduction in double-layered thin films exposed to ultrashort-pulsed lasers, *Int. J. Heat Mass Transf.* 178 (2021) 121616.
- [37] M. Raissi, P. Perdikaris, G.E. Karniadakis, Physics-informed neural networks: a deep learning framework for solving forward and inverse problems involving nonlinear partial differential equations, *J. Comput. Phys.* 378 (2019) 686–707.
- [38] B. Zakeri, A.K. Monsefi, B. Darafarin, Deep learning prediction of heat propagation on 2-D domain via numerical solution, *Data Sci.: From Research to Application* 45 (2020) 161–174.
- [39] L. Ruthotto, E. Haber, Deep neural networks motivated by partial differential equations, *J. Math. Imaging Vis.* 62 (2020) 352–364.
- [40] G. Pang, L. Lu, G.E. Karniadakis, PINNs: fractional physics-informed neural networks, *SIAM J. Sci. Comput.* 41 (2019) A2603–A2626.
- [41] X.I.A. Yang, S. Zafar, J.-X. Wang, H. Xiao, Predictive large-eddy-simulation wall modeling via physics-informed neural networks, *Phys. Rev. Fluids* 4 (2019) 034602.
- [42] G.P.P. Pun, R. Batra, R. Ramprasad, Physically informed artificial neural networks for atomistic modeling of materials, *Nat. Commun.* 10 (2019) 2339.
- [43] Y. Chen, L. Lu, G.E. Karniadakis, L.D. Negro, Physics-informed neural networks for inverse problems in nano-optics and metamaterials, *Opt. Express* 28 (2020) 11618–11633.
- [44] T. Kadeethum, T.M.J. Argensen, H.M. Nick, Physics-informed neural networks for solving nonlinear diffusivity and Biot's equations, *PLoS One* 15 (2020) 0232683.
- [45] S. Goswami, C. Anitescu, S. Chakraborty, T. Rabczuk, Transfer learning enhanced physics informed neural network for phase-field modeling of fracture, *Theor. Appl. Fract. Mech.* 106 (2020) 102447.
- [46] Q. He, D.B. Solano, G. Tartakovsky, A.M. Tartakovsky, Physics-informed neural networks for multiphysics data assimilation with application to subsurface transport, *Adv. Water Resour.* 141 (2020) 103610.
- [47] Z. Fang, J. Zhan, A physics-informed neural network framework for PDEs on 3D surfaces: time independent problems, *IEEE Access* 8 (2020) 26328–26335.
- [48] G. Kissas, Y. Yang, E. Hwuang, W.R. Witschey, J.A. Detre, P. Perdikaris, Machine learning in cardiovascular flows modeling: predicting arterial blood pressure from non-invasive 4D flow MRI data using physics-informed neural networks, *Comput. Methods Appl. Mech. Eng.* 358 (2020) 112623.
- [49] A.M. Tartakovsky, C.O. Marrero, P. Perdikaris, G.D. Tartakovsky, D.B. Solano, Physics-informed deep neural networks for learning parameters and constitutive relationships in subsurface flow problems, *Water Resour. Res.* 56 (2020) 026731.
- [50] C. Rao, H. Sun, Y. Liu, Physics-informed deep learning for incompressible laminar flows, *Theor. Appl. Mech. Lett.* 10 (2020) 207–212.
- [51] V. Dwivedi, B. Srinivasan, Physics informed extreme learning machine (PIELM) a rapid method for the numerical solution of partial differential equations, *Neurocomputing* 391 (2020) 96–118.
- [52] H. Wessels, C. Weißenfels, P. Wriggers, The neural particle method - an updated lagrangian physics informed neural network for computational fluid dynamics, *Comput. Methods Appl. Mech. Eng.* 368 (2020) 113127.
- [53] A. Ghaderi, V. Morovati, R. Dargazany, A physics-informed assembly of feed-forward neural network engines to predict inelasticity in cross-linked polymers, *Polymers* 12 (2020) 2628.
- [54] R. Zhang, Y. Liu, H. Sun, Physics-informed multi-LSTM networks for metamodelling of nonlinear structures, *Comput. Methods Appl. Mech. Eng.* 369 (2020) 113226.
- [55] K. Champion, P. Zheng, A.Y. Aravkin, S.L. Brunton, J.N. Kutz, A unified sparse optimization framework to learn parsimonious physics-informed models from data, *IEEE Access* 8 (2020) 169259–169271.
- [56] A. Li, R. Chen, A.B. Farmani, Reaction diffusion system prediction based on convolutional neural network, *Sci. Rep.* 10 (2020) 3894.
- [57] S. Pan, K. Duraisamy, Physics-informed probabilistic learning of linear embeddings of nonlinear dynamics with guaranteed stability, *SIAM J. Appl. Dyn. Syst.* 19 (2020) 480–509.
- [58] A.T. Mohan, D. Tretiak, M. Chertkov, D. Livescu, Spatio-temporal deep learning models of 3D turbulence with physics informed diagnostics, *J. Turbul.* 21 (2020) 484–524.
- [59] X. Zhao, K. Shirvan, R.K. Salko, F. Guo, On the prediction of critical heat flux using a physics-informed machine learning-aided framework, *Appl. Therm. Eng.* 164 (2020) 114540.
- [60] E. Qian, B. Kramer, B. Peherstorfer, K. Willcox, Lift and learn: physics-informed machine learning for large-scale nonlinear dynamical systems, *Phys. D* 406 (2020) 132401.
- [61] L. Lu, X. Meng, Z. Mao, G.E. Karniadakis, DeepXDE: a deep learning library for solving differential equations, *SIAM Rev.* 63 (2021) 208–228.
- [62] H. Haghighat, R. Juanes, SciANN: a Keras/TensorFlow wrapper for scientific computations and physics-informed deep learning using artificial neural networks, *Comput. Methods Appl. Mech. Eng.* 373 (2021) 113552.
- [63] C.L. Wight, J. Zhao, Solving Allen–Cahn and Cahn–Hilliard equations using the adaptive physics informed neural networks, *Commun. Comput. Phys.* 29 (2021) 930–954.
- [64] H. Gao, L. Sun, J.X. Wang, Phygeonet: physics-informed geometry-adaptive convolutional neural networks for solving parameterized steady-state PDEs on irregular domain, *J. Comput. Phys.* 428 (2021) 110079.
- [65] C. Song, T. Alkhalifah, U.B. Waheed, Solving the frequency-domain acoustic VTI wave equation using physics-informed neural networks, *Geophys. J. Int.* 225 (2021) 846–859.
- [66] Q. Zhu, Z. Liu, J. Yan, Machine learning for metal additive manufacturing: predicting temperature and melt pool fluid dynamics using physics-informed neural networks, *Comput. Mech.* 67 (2021) 619–635.
- [67] C. Cheng, G.T. Zhang, Deep learning method based on physics informed neural network with ResNet block for solving fluid flow problems, *Water* 13 (2021) 3040423.
- [68] X. Lei, Z. Yang, J. Yu, J. Zhao, Q. Gao, H. Yu, Data-driven optimal power flow: a physics-informed machine learning approach, *IEEE Trans. Power Syst.* 36 (2021) 346–354.
- [69] D. Kingma, J. Ba, Adam: A Method for Stochastic Optimization, *ICLR*, 2015.
- [70] D.C. Liu, J. Nocedal, On the limited memory BFGS method for large scale optimization, *Math. Program.* 45 (1989) 503–528.
- [71] A. Suslova, A. Hassanein, Numerical simulation of ballistic electron dynamics and heat transport in metallic targets exposed to ultrashort laser pulse, *J. Appl. Phys.* 124 (2018) 065108.
- [72] C.Y. Ho, M.Y. Wen, B.C. Chen, Y.H. Tsai, Non-fourier two-temperature heat conduction model used to analyze ultrashort-pulse laser processing of nanoscale metal film, *J. Nanosci. Nanotechnol.* 14 (2014) 24758069.
- [73] P. Bresson, J.-F. Bryche, M. Besbes, J. Moreau, P.-L. Karsenti, P.G. Charette, D. Morris, M. Canva, Improved two-temperature modeling of ultrafast thermal and optical phenomena in continuous and nanostructured metal films, *Phys. Rev. B* 102 (2020) 155127.
- [74] P. Hopkins, P. Norris, Contribution of ballistic electron transport to energy transfer during electron-phonon nonequilibrium in thin metal films, *ASME J. Heat Transf.* 131 (2009) 043208.
- [75] J. Hohlfield, S.S. Wellershoff, J. Gudde, U. Conrad, V. Jahnke, E. Matthias, Electron and lattice dynamics following optical excitation of metals, *Chem. Phys.* 251 (2000) 237–258.
- [76] T.Q. Qiu, T. Juhasz, C. Suarez, W.E. Bron, C.L. Tien, Femtosecond laser heating of multi-layer metals II. Experiments, *Int. J. Heat Mass Transf.* 37 (1994) 2799–2808.
- [77] S.L. Sobolev, Nonlocal two-temperature model: application to heat transport in metals irradiated by ultrashort laser pulses, *Int. J. Heat Mass Transf.* 94 (2016) 138–144.
- [78] S.L. Sobolev, Equations of transfer in non-local media, *Int. J. Heat Mass Transf.* 37 (1994) 2175–2182.
- [79] S.L. Sobolev, The local-nonequilibrium temperature field around the melting and crystallization front induced by picosecond pulsed laser irradiation, *Int. J. Thermophys.* 17 (1996) 1089–1097.
- [80] S.L. Sobolev, Local non-equilibrium transport models, *Phys. Usp.* 40 (1997) 1043–1053.
- [81] S.L. Sobolev, Nonlocal diffusion models: application to rapid solidification of binary mixtures, *Int. J. Heat Mass Transf.* 71 (2014) 295–302.
- [82] D. Jou, V.A. Cimmelli, A. Sellitto, Nonlocal heat transport with phonons and electrons: application to metallic nanowires, *Int. J. Heat Mass Transf.* 55 (2012) 2338–2344.
- [83] R.A. Guyer, J.A. Krumhansl, Solution of the linearized phonon Boltzman equation, *Phys. Rev.* 148 (1966) 766–778.
- [84] D.D. Joseph, L. Preziosi, Heat waves, *Rev. Mod. Phys.* 61 (1989) 41–73.
- [85] A. Sellitto, F.X. Alvarez, D. Jou, Geometrical dependence of thermal conductivity in elliptical and rectangular nanowires, *Int. J. Heat Mass Transf.* 55 (2012) 3114–3120.
- [86] G. Lebon, Heat conduction at micro and nanoscales: a review through the prism of extended irreversible thermodynamics, *J. Non-Equilib. Thermodyn.* 39 (2014) 35–59.
- [87] Y. Guo, M. Wang, Phonon hydrodynamics and its applications in nanoscale heat transport, *Phys. Rep.* 595 (2015) 1–44.
- [88] N. Challamel, C. Grazide, V. Picandet, A. Perrot, Y. Zhang, A nonlocal fourier's law and its application to the heat conduction of one-dimensional and two-dimensional thermal lattices, *C. R. Méc.* 344 (2016) 388–401.
- [89] H. Machraf, Extended Non-Equilibrium Thermodynamics From Principles to Applications in Nanosystems, CRC Press, Boca Raton, 2019.
- [90] V.A. Cimmelli, Different thermodynamic theories and different heat conduction laws, *J. Non-Equilib. Thermodyn.* 34 (2009) 299–333.
- [91] P. Ván, T. Fülöp, Universality in heat conduction theory - weakly nonlocal thermodynamics, *Ann. Phys.* 524 (2012) 470–478.
- [92] B. Rethfeld, D.S. Ivanov, M.E. García, Modelling ultrafast laser ablation, *J. Phys. D* 50 (2017) 193001.
- [93] W.E. Frazier, Metal additive manufacturing: a review, *J. Mater. Eng. Perform.* 23 (2014) 1917–1928.
- [94] E.G. Gamaly, A.V. Rode, Physics of ultra-short laser interaction with matter: from phonon excitation to ultimate transformations, *Prog. Quantum Electron.* 37 (2013) 215–323.
- [95] J.S. Jin, J.S. Lee, O. Kwon, Electron effective mean free path and thermal conductivity predictions of metallic thin films, *Appl. Phys. Lett.* 92 (2008) 171910.
- [96] D. Gall, Electron mean free path in elemental metals, *J. Appl. Phys.* 119 (2016) 085101.
- [97] D.Y. Tzou, W. Dai, Thermal lagging in multi-carrier system, *Int. J. Heat Mass Transf.* 52 (2009) 1206–1213.
- [98] W. Dai, A hyperbolic microscopic model and its numerical scheme for thermal analysis in an N-carrier system, *Int. J. Heat Mass Transf.* 52 (2009) 2379–2389.
- [99] W. Dai, F. Zhu, D.Y. Tzou, A stable finite difference scheme for thermal analysis in an N-carrier system, *Int. J. Therm. Sci.* 48 (2009) 1530–1541.